Final Draft
of the original manuscript:

Srinivasan, A.; Dieringa, H.; Mendis, C.L.; Huang, Y.; Rajesh Kumar, R.; Kainer, K.U.; Hort, N.:

Creep behavior of Mg–10Gd–xZn (x=2 and 6wt%) alloys

In: Materials Science and Engineering A (2015) Elsevier

DOI: 10.1016/j.msea.2015.09.113

Creep behavior of Mg–10Gd–xZn (x = 2 and 6 wt%) alloys

A. Srinivasan[1,2] and H. Dieringa[1], C.L. Mendis[1], Y. Huang[1], R. Rajesh Kumar[2], K.U. Kainer[1], N. Hort[1]

[1]Magnesium Innovation Center, Helmholtz-Zentrum Geesthacht, Geesthacht, Germany
[2]CSIR-National Institute for Interdisciplinary Science and Technology, Pappanamcode (P.O), Thiruvananthapuram 695 019, India

Abstract

Creep behavior of Mg–10Gd–xZn alloys was investigated with two Zn contents, 2 and 6 wt%. The as cast microstructure of alloys contained (Mg, Zn)3Gd phase at the interdendritic regions and long period stacking ordered (LPSO) phase in the matrix. Increase in the Zn content from 2% to 6%, increased the volume fraction and morphology of second phase [$(Mg,Zn)_3Gd$]. Creep testing at 250 and 300 °C with stress levels between 50 and 120 MPa indicated that increase in Zn content or temperature reduced the creep performance of the Mg–10Gd–xZn alloys. The minimum creep rate of Mg–10Gd–2Zn was one order less that of Mg–10Gd–6Zn. Dynamic precipitation was found in both the alloys during creep deformation at 250 °C and strengthened the alloys: prismatic platelets (Mg_5Gd) were observed perpendicular to the LPSO phase in Mg–10Gd–2Zn alloy whereas basal oval precipitates (ternary composition) parallel to the LPSO occurred in Mg–10Gd–6Zn alloy. The dynamic precipitates were not observed in alloys during creep at 300 °C. Ternary bulk precipitates at the LPSO phase was observed in both alloys and at all testing conditions which facilitated the cracking during deformation. More continuous second phase at the interdendritic boundaries facilitated easy cracking in Mg–10Gd–6Zn alloy and hence reduced the creep performance.

1 Introduction

Magnesium alloys have great potential for structural applications due to their low density and high specific properties. However, the applications are limited due to their lower elevated temperature properties, especially creep [1]. The most widely used commercial Mg alloys belong to the Mg–Al group (AZ91) and only find applications in components subjected to low stresses or low temperatures (below 100 °C). Last four to five decades witnessed significant R&D efforts in the development of many new die cast and gravity cast Mg alloys with better creep resistance. Among various alloying elements providing high creep resistant to Mg alloys, RE elements are proved to be the most effective [2–4]. Rare earths (RE) additions are used both in die cast alloys as well as in gravity cast alloys. For instance, AE42 (Mg–4%Al–2%RE) is one such alloy used for die casting applications whose creep properties are considered to be the bench mark for new die casting alloys. On the other hand, ZE41 (Mg–4%Zn–1%RE–0.4Zr) is a creep resistant Mg alloy used in gravity casting for high temperature applications.

Normally, RE is added to Mg in the form of mishmetal (MM), which is a La or Ce based RE mixture. In general, the RE elements can be classified into two groups according to their solubility in Mg: (i) low soluble (Nd, Ce, La) (ii) high soluble (Y, Gd, Dy) elements. WE43 (Mg–4%Y–3%RE), one of the Mg alloys used for aerospace applications, consists of high soluble Y and offering high creep properties. Based on the performance of Y in Mg alloys, recently, magnesium alloys with heavy and high solubility RE such as Gd, Dy are subject of scientific investigations for various applications [5–6]. Gd addition to Mg alloys is being investigated for the possibility of developing new magnesium alloys with a good combination of mechanical and corrosion properties.

It has been reported that binary Mg–Gd alloys have better creep resistance than that of the commercially used WE43 alloy, and high creep resistant QE22 alloy [6]. Many experimental alloys based on Mg– Gd–Y, Mg–Gd–Y–Nd, Mg–Gd–Zn, and Mg–Gd–Y–Zn systems have been developed, and their microstructure and mechanical properties are investigated [7–12]. Among these systems, Mg–Gd–Zn is one of the interesting systems as its microstructure consists of different phases, such as I, W, Z and laves phases, depending on the ratio of Zn and Gd resulting in different mechanical behavior [13,14]. Thus, the mechanical properties of these alloys can be tailored accordingly by altering the Zn and Gd contents. Formation of different phases in this system depends not only on the alloy compositions but also on the heat treatment [11].

Recently, the microstructure, mechanical and corrosion properties of Mg–Gd–Zn alloys were characterized in detail [15,16]. In the present study, the creep behavior of these alloys was investigated and correlated with their microstructures.

Nominal composition (wt%) and alloy code	Analyzed compositions (wt%)				
	Gd	Zn	Fe	Ni	Cu
Mg10Gd3Zn (alloy 1)	9.11	2.29	0.0022	0.0002	0.0042
Mg10Gd6Zn (alloy 2)	8.65	6.661	0.0023	0.0002	0.0050

Table 1: Analyzed chemical compositions of the alloys.

2 Materials and Methods

2.1 Casting

The required alloys, Mg–10%Gd–2%Zn and Mg–10%Gd–6%Zn (all are in wt% unless otherwise stated), for the present investigation were prepared in a resistance tilt furnace under a protective gas mixture of Ar þ 0.2% SF_6. Pure Mg, Zn and Gd ingots were used to prepare the alloys. Initially Mg and Zn were melted in boron-nitride (BN) coated mild steel crucible, and Gd was added into the melt at around 770 °C. After the addition, the melt was stirred mechanically at 200 rpm for 30 min, for the complete dissolution of Gd and to achieve uniform compositions in the melt.

The melt was poured into a preheated (350 °C) metallic round mould with an inner diameter of 100 mm and a height of 400 mm attached with a sprue at the top. The analyzed chemical compositions of the major alloying elements and the alloy codes for the easy reference are presented in Table 1. The Zn was analyzed using optical emission spectroscopy (OES) while Gd was analyzed with X-ray fluorescence analysis (XRF). The impurities contents were analyzed using inductively coupled plasma optical emission spectroscopy (ICP-OES).

2.2 Microstructure

Samples for the microstructural studies were prepared by grinding them on different grades of SiC papers from 80 to 2400 grits, and then, polishing with 0.05 mm colloidal silica (OPS). The samples were etched in a solution of 6 g picric acid, 5 ml acetic acid, 10 ml distilled water and 100 ml ethanol, and examined under a light microscope (Reichert-Jung MeF3) attached with a digital camera with analySIS pro software. Polished samples were also examined in a Zeiss Ultra scanning electron microscope (SEM) attached with energy dispersive X-ray spectroscopy (EDXS). Selected samples were examined with transmission electron microscopy (TEM). The specimens for TEM were mechanically ground to about 400 mm in thickness and then 3 mm diameter discs were cut using an abrasive slurry disc cutter. These discs were mechanically ground to 120 μm in thickness, and fur-

ther thinned by twin-jet electro polishing in a solution of 1.5% $HClO_4$ and 98.5% ethanol at -45 °C and 40 V. The TEM examinations were conducted on a Philips CM 200 operating at 200 kV.

2.3 Creep testing

M10 threaded round samples with a gauge length of 30 mm and a diameter of 6 mm were machined out from the castings with spark erosion technique followed by turning. Creep tests under constant tensile stresses were conducted at ATS lever arm creep test systems in air at stresses between 50 and 120 MPa and constant temperatures of 250 or 300 °C. The temperatures of the sample were monitored by placing two separate thermocouples close to the specimen, and the sample temperature was controlled with an accuracy of ± 1 °C. Two extensometers connected to a measuring unit were used to measure the strain on the samples during the test. Duplicated test was conducted for each condition and average value is reported.

3 Results

3.1 As cast microstructure

The microstructure of alloy 1 exhibited columnar dendrites (Fig. 1(a)), and at a higher magnification, the microstructure (Fig. 1 (b)) showed two different types of phases located mostly at the interdendritic regions. The major phase marked as 'A' in Fig. 1 (b) had rib bone like morphology. The other phase, marked as 'B', was relatively smaller in size, and was a solid block. EDXS analysis of the phase 'A' suggested that the phase contained slightly higher Gd content than Zn. The typical composition of the phase was 56.97 at% Mg, 21.97 at% Gd, 19.47 at% Zn.

The TEM analysis of the phase confirmed that the phase was face centered cubic (fcc) Mg3Gd with lattice parameter 'a' = 0.726 nm, and identified as $(Mg,Zn)_3Gd$ phase [15]. The small particles, which were low in volume fraction (marked as 'B' in Fig. 1(b)), contained equal amount of Gd and Zn content (81.49 at% Mg-8.62 at% Gd-8.72 at% Zn). This phase was similar to $Mg_{12}GdZn$ phase, which is normally referred as Z or X phase containing LPSO structure [10]. In contrast to alloy 1, the microstructure of alloy 2 consisted of a continuous network of rib bone like phase (Fig. 1(c) and (d)). T

he EDXS spectra recorded from particles showed that the Zn content was slightly higher than the Gd, and the Zn/Gd ratio was close to 1.5. TEM analysis suggested that the phase was similar to that observed in alloy 1 but with a lattice parameter, a = 0.732 nm [15]. The TEM investigation also confirmed the

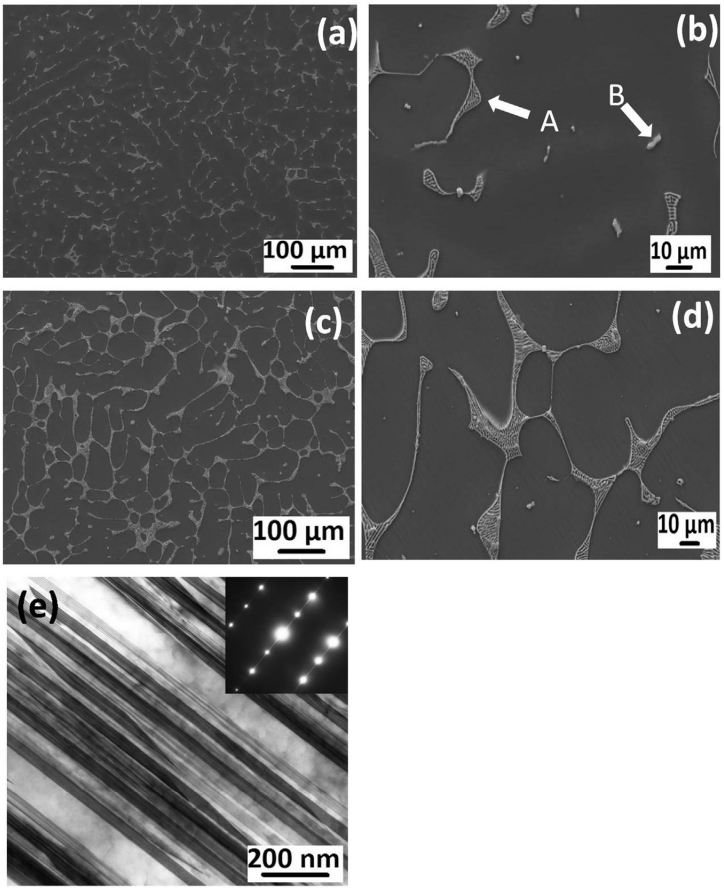

Figure 1: Microstructure of as cast alloys: (a) and (b) alloy 1, (c) and (d) alloy 2, (e) TEM photograph of alloy 1 showing LPSO.

Testing conditions		Alloy 1		Alloy 2	
Temperature °C	Stress (MPa)	min. creep rate (s^{-1})	testing time (h)	min. creep rate (s^{-1})	testing time (h)
250	70	2.22 x 10^{-9}	948.65 (f)	1.47 x 10^{-8}	351.25 (s)
	80	1.05 x 10^{-8}	655.30 (f)	2.78 x 10^{-8}	445.7 (f)
	100	2.20 x 10^{8}	134.45 (f)	1.70 x 10^{-7}	23.94 (f)
	120	2.2 x 10^{-7}	11.229	8.01 x 10^{-7}	6.45 (f)
300	50	5.55 x 10^{-9}	383.45 (s)	1.15 x 10^{-7}	134.87 (s)
	60	4.98 x 10^{-8}	100.56 (f)	4.01 x 10^{-7}	38.04 (f)
	70	1.66 x 10^{-7}	46.65 (f)	1.08 x 10^{-6}	17.35 (f)
	80	3.14 x 10^{-7}	25.63 (f)	2.70 x 10^{-6}	8.87 (f)
	90	1.34 x 10^{-6}	14.71 (f)	6.30 x 10^{-6}	1.37 (f)

f - The test ran until the sample fractured)text
s - The test stopped after the min. creep rate was reached.

Table 2: Creep properties of alloys at different temperatures and stresses.

presence of fine lamellar LPSO phases in both the alloys within the Mg grains. A typical micrograph of LPSO in alloy 2 is shown in Fig. 1(e).

3.2 Creep properties

Table 2 shows the results of the creep testing at different temperatures and stresses. Most of the tests were conducted until the samples fractured; however, few were stopped in the defined steady state creep region. Fig. 2 shows typical creep curves of the alloys tested at 250 and 300 °C under 70 and 80 MPa load for comparison. The creep performance of alloy 1 was better than that of alloy 2 at all the tested temperature and stress conditions. In most of the cases, for a similar testing condition, the minimum creep rate of the alloy 2 was one order of magnitude higher than that of alloy 1 (Table 2). For instance, the alloy 1 exhibited a secondary creep rate of 2.2 x 10^{-9} s^{-1} at 250 °C and 70 MPa, whereas the alloy 2 exhibited a minimum creep rate of 1.47 x 10^{-8} s^{-1}. These results indicate that the increase in Zn content in Mg–10Gd–xZn alloy from 2% to 6% significantly reduced the creep resistance of the alloy.

The creep data of the alloys are also shown in strain rate vs. time normalized to the fracture time and strain rate vs. strain plots in Fig. 3 and Fig. 4, respectively. The creep curves show the typical behavior. The creep rate reduced drastically during the primary creep stage, and reached a minimum or constant steady state

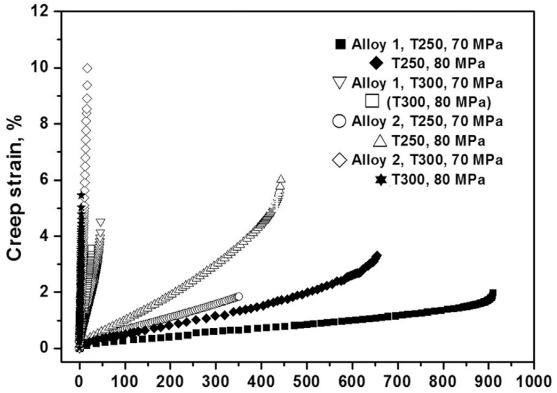

Figure 2: Typical creep curves of alloys at different temperatures and stresses.

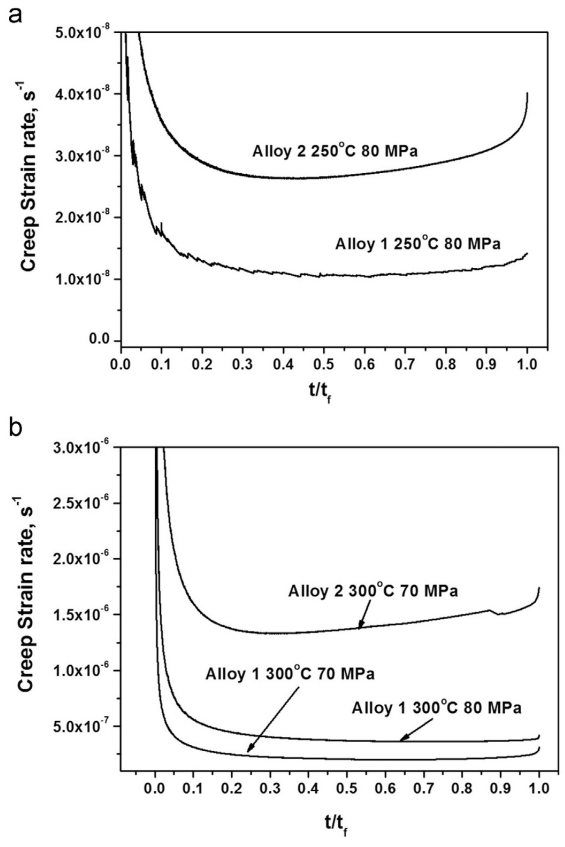

Figure 3: Creep data of the alloys represented in creep rate verses time normalized with fracture life at different temperatures (a) 250 °C (b) 300 °C.

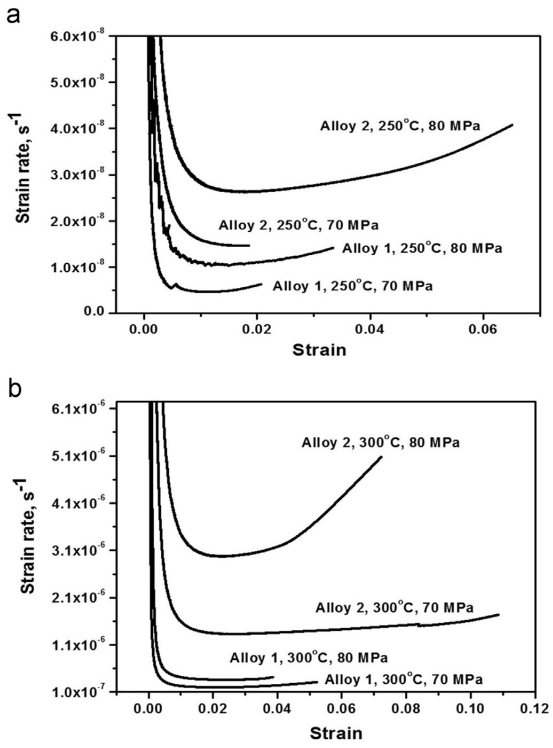

Figure 4: Creep data of the alloys represented in creep rate verses strain at different temperatures (a) 250 °C (b) 300 °C.

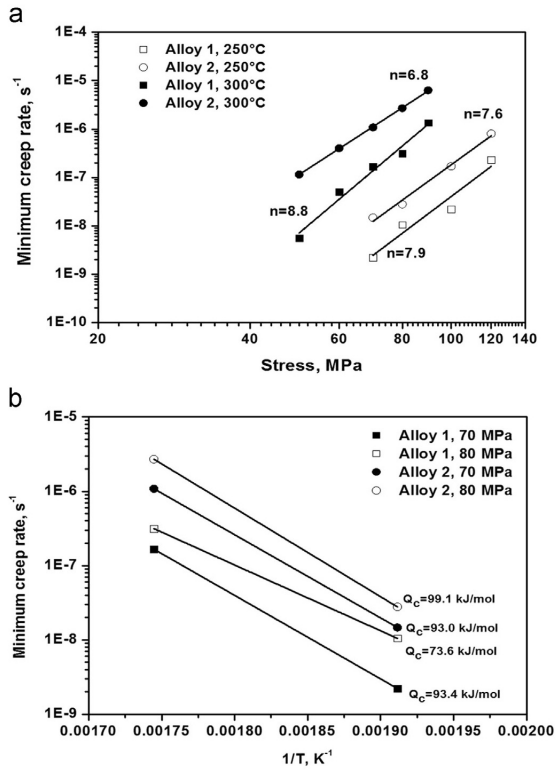

Figure 5: (a) Minimum creep rate plotted against applied stress for the alloys (b) temperature dependence on minimum creep rate of alloys.

region before it increased again at a faster rate in the tertiary creep region. The tertiary creep region was more apparent in alloy 2(Fig. 3). The alloy 2 did not exhibit clear steady state creep region; once the creep rate reached a minimum, it continuously increased until fracture. Compared with alloy 2, alloy 1 had a longer primary creep region and significantly lower minimum creep rate. For instance, alloy 1 reached its minimum creep rate of 1.06 x 10^{-8} s^{-1} after 45% of its total fracture life at 250 °C with 80 MPa (Fig. 3(a)). In contrast, alloy 2 reached its minimum creep rate (2.78 x 10^{-8} s^{-1}) after 33% of its total life at an applied stress of 80 MPa. In addition, the total fracture strains of the alloys at similar testing conditions were also noticeably different (Fig. 4).

In general, alloy1 exhibited lower creep strain to fracture compared with that of alloy 2 in all the testing conditions. The increase in the creep deformation temperature from 250 °C to 300 °C significantly reduced the creep resistance in both the alloys. For instance, the secondary creep rate of the alloy 1 increased from 2.22 x 10^{-9} s^{-1} at 250 °C to 1.7 x 10^{-7} s^{-1} at 300 °C for a stress of 70 MPa, which is two orders of magnitudes higher, while the creep life drastically decreased from $\sim$ 900 h to $\sim$ 48 h ((Figs. (2) and 3)). Similarly, the creep rate increased significantly when the load increased from 70 to 80 MPa at 250 °C for alloy 1. However, the change in creep rate was not so significant in case of similar load change in alloy 2.

The stress dependence on the strain rate can be obtained from the stress exponent n, defined as:

$$n = (\frac{\partial ln\dot{\epsilon}}{\partial ln\sigma})_{\sigma} \tag{1}$$

where T is the absolute temperature. The logarithmic stress vs. min. creep rate plots for the alloys at 250 and 300 °C is shown in Fig. 5(a). The calculated n value changed from 7.9 at 250 °C to 8.8 at 300 °C for the alloy 1, whereas it changed from 7.6 to 6.8 for alloy 2. Similarly, the activation energy (Q) can also be calculated using the following equation:

$$Q = -R\frac{\partial ln\dot{\epsilon}}{\partial \frac{1}{T}} \tag{2}$$

where R is the gas constant. Fig. 5(b) shows the Arrhenius plot for the alloys where the logarithmic minimum creep rates were plotted against the inverse of testing temperatures. The calculated Q value for alloy 1 was in the range of 93.4 and 73.6 kJ/mol at the stress values of 70 and 80 MPa, respectively. Similarly, Q value changed from 93 to 99.1 kJ/mol for alloy 2 with the change in the applied stress form 70 to 80 MPa. 3.3. Microstructure after creep Microstructures of longitudinal cross section near the fracture surface of creep tested alloys at different

conditions were analyzed. The optical microstructure of alloy 1 crept at 250 °C with 70 MPa shown in Fig. 6(a) shows the following features after creep:

- platelet precipitates around the second phases (marked as 'a')
- bulk shaped precipitates in the matrix (marked as 'b')
- cavities in the matrix along the LPSO phase (marked as 'c') (iv) damaged grain boundary second phases, $(Mg,Zn)_3Gd$, (marked as 'd').

These features are more clearly viable with high magnification micrographs shown in Fig. 6(b–d). The platelet precipitates formed mainly along the interdendritic regions and near the grain boundary phase i.e. at eutectic regions (Fig. 6(b)). The precipitates orientated with three definite directions with approximately 60° to each other. Given the 60° rotation between the precipitates, the grain in Fig. 6(b) might be oriented close to the [0001]Mg zone axis.

The bulk shaped precipitates also aligned along with the LPSO phases in the matrix suggesting that either these phases might have nucleated near the LPSO phase from the solutes in the matrix or formed due to diffusion mechanisms associated the coarsening of LPSO during creep exposure (Fig. 6(c)). Both bulk shaped precipitates and LPSO formed on the basal planes. The cavities in the matrix had a definite orientation; they aligned along the LPSO phase in the matrix (Fig. 6(d)). Moreover, it appears that the cracks formed at the bulk phase in the matrix. Multiple cracks in the grain boundary phases located near the fracture region are shown as (marked as 'd')in Fig. 6(e).

It was also observed that away from the fracture region, the grain boundary phases were less affected (micrograph is not shown here). Similar microstructural features were also observed with the alloy tested at 250 °C with 80 MPa and shown in Fig. 6(f). There was an increase in the number and size of cavities near the fracture region. The bulk shaped phase along the LPSO was coarser than that observed in the microstructure of creep deformed alloy at same temperature but with 70 MPa (marked as 'b' in Fig. 6(f)) suggesting that the formation of bulk phase and cracks along it accelerated with increase in applied stress. It should be noted that the platelet precipitates were relatively finer in the alloy tested at 80 MPa (marked as 'a' in Fig. 6(f)) compared with that observed in the samples tested at same temperature but with 70 MPa which was due to the difference in the rupture life (Table 2). Interestingly, prismatic platelets were not observed in alloy 2.

Typical microstructure of the alloy 2 creep tested at 250 °C with 80 MPa shown in Fig. 7 exhibits more cracks at the interface between the second phase and the matrix than the cracks in the matrix along the LPSO phase. This observation suggests that the increase in the grain boundary cavities due to the increase

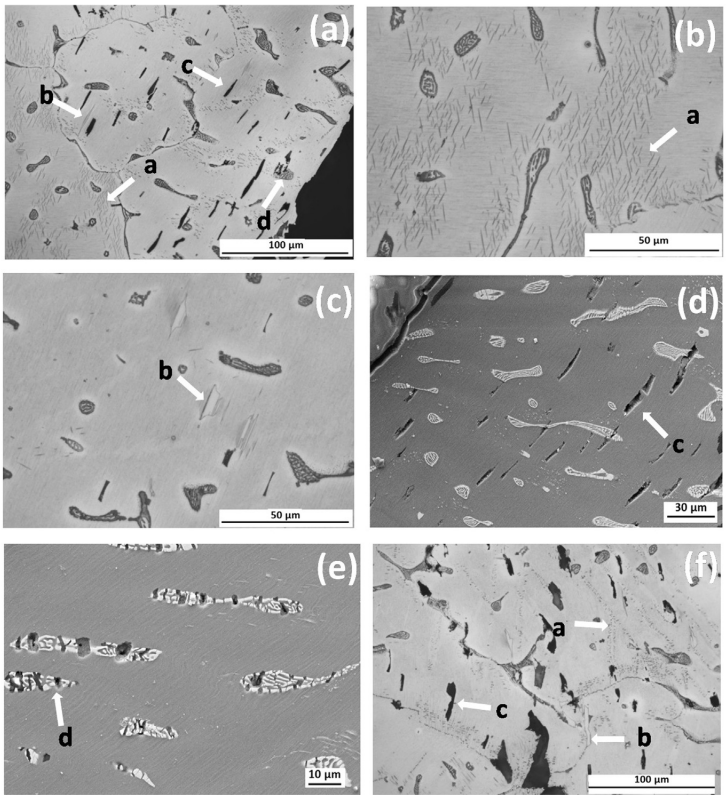

Figure 6: Microstructure of alloy 1 after creep tested at 250 °C with different initial stresses: (a–e) at 70 MPa showing (a) overall feature (b) dynamic precipitates (c) bulk precipitates (d) cavities along LPSO (e) multiple cracking of intermetallic particles; (f) at 80 MPa.

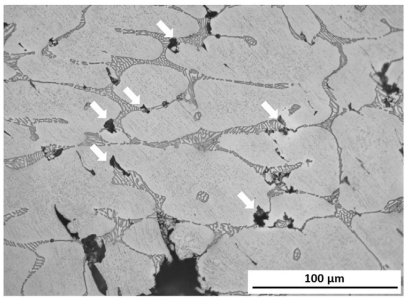

Figure 7: Microstructure of alloy 2 after creep tested at 250 °C and 80 MPa.

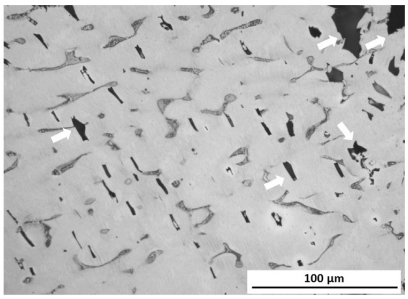

Figure 8: Microstructure of alloy 1 after creep tested at 300 °C and 70 MPa.

in the volume fraction of grain boundary phase played a major role in the poor creep performance of alloy 2. The microstructures of both alloys deformed at the higher temperature (300 °C) did not contain the dynamic precipitates. The typical microstructure of the alloy 1 deformed at 300 °C with 70 MPa shown in Fig. 8 contained a large number of cavities aligned along the LPSO phase in the matrix near the fracture region. Compared with the microstructure of alloy 1 tested with 70 MPa but at 250 °C(Fig. (6)), the severity of cavities in the matrix near the fracture area was more prominent at 300 °C. These results suggest that an increase in the volume fraction of bulk shaped phase along the LPSO at the higher temperature.

The EDXS analysis of the bulk shaped phase particles revealed that they consisted of almost equal amounts of Gd and Zn (3.21 at%Gd and 2.21 at% Zn), whereas the platelet precipitates in the interdendritic region was enriched with higher concentration of Gd than Zn (4.14 at% Gd and 0.32 at% Zn). It should be noted that the surrounding matrix contributed to the measurement of the composition of the precipitates, in particularly with the thin platelet precipitates as the interaction volume of the electron beam was larger than the precipitate volume investigated.

To identify the precipitates that formed during creep deformation in the alloys investigated, selected samples were analyzed with TEM. Since the resultant microstructure after creep deformation is due to the combined effects of temperature and stress, alloy samples subjected to similar thermal treatments but without an applied stresses were also investigated for comparison.

Fig. 9 show the TEM micrograph of alloy 1 deformed at 250 °C with 70 MPa for 948 h and of a sample from the same alloy heat treated for 1000 h at 250 °C. No precipitates were observed in the heat treated sample (Fig. 9(a)) whereas coarse platelet precipitates near the grain boundary phases were detected in the crept sample (Fig. 9(b)). Although, the higher magnification images of the heat treated samples did not show evidence of any dislocations in between LPSO structures (Fig. 9(c)), dislocations bridging layers of LPSO phase were observed in crept

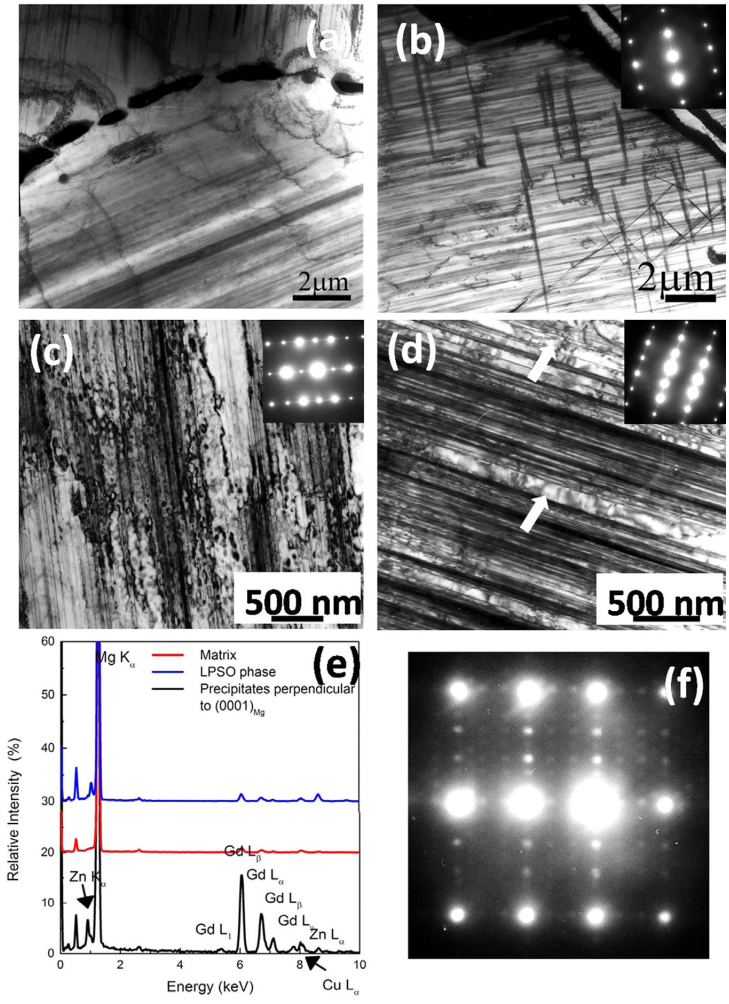

Figure 9: TEM micrographs of alloy 1: (a) and (c) subjected to only temperature at 250 °C for 1000 h (b) and (d) crept at 250 °C and 70 MPa; (e) X-ray analysis of phases in alloy 1; (f) SAD pattern of β-Mg_5Gd.

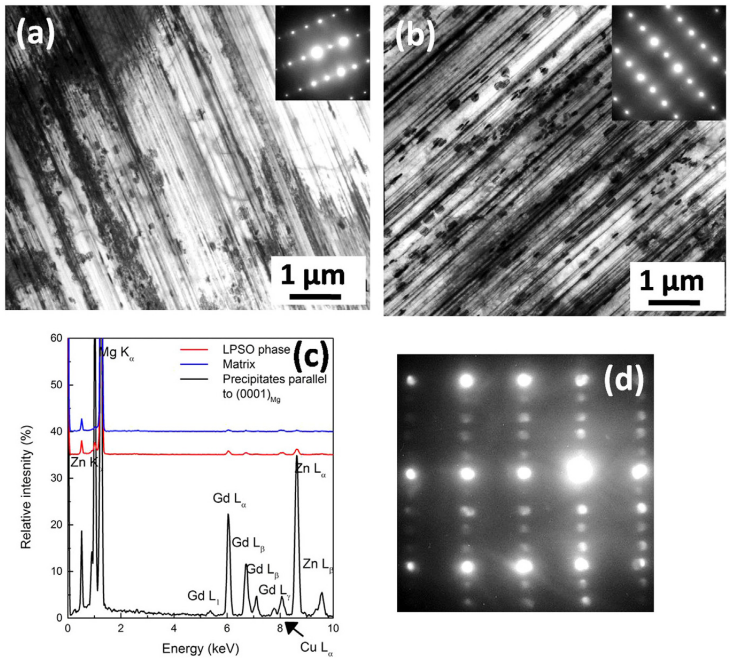

Figure 10: TEM micrographs of alloy 1: (a) subjected to only temperature at 300 °C for 48 h (b) crept at 300 °C and 70 MPa.

sample (Fig. 9(d)). This observation suggests that the LPSO phase effectively restricted the movement of the dislocations during creep deformation.

The results of EDXS analysis (Fig. 9(e)) and the electron micro-diffraction analysis (Fig. 9(f)) of the precipitates perpendicular to the basal planes (perpendicular to LPSO) confirm that these prismatic platelets were equilibrium Mg_5Gd phase. The results of TEM analysis also show that no Mg_5Gd precipitates formed in alloy 1 when the creep deformation temperature increased to 300 °C, and there were no appreciable differences between the crept and the heat treated samples except that the crept alloy contained few isolated dislocations trapped between the LPSO structures [Fig. 10].

The microstructure of alloy 2 crept at 250 °C with 80 MPa and a sample heat treated for a similar length of time (445 h) without an applied stress are shown in Fig. 11. No platelet precipitates perpendicular to the LPSO was observed in the samples; however, both samples (crept sample and heat treated sample) contained oval shaped precipitates parallel to the basal planes (parallel to LPSO structure). The density of the basal precipitates was significantly higher in the sample subjected to creep deformation, Fig. 11 (b), compared to the sample heat treated at 250 °C for similar length of time, Fig. 11 (a). The size of the particle in the crept sample was also coarser than those found in the heat treated samples.

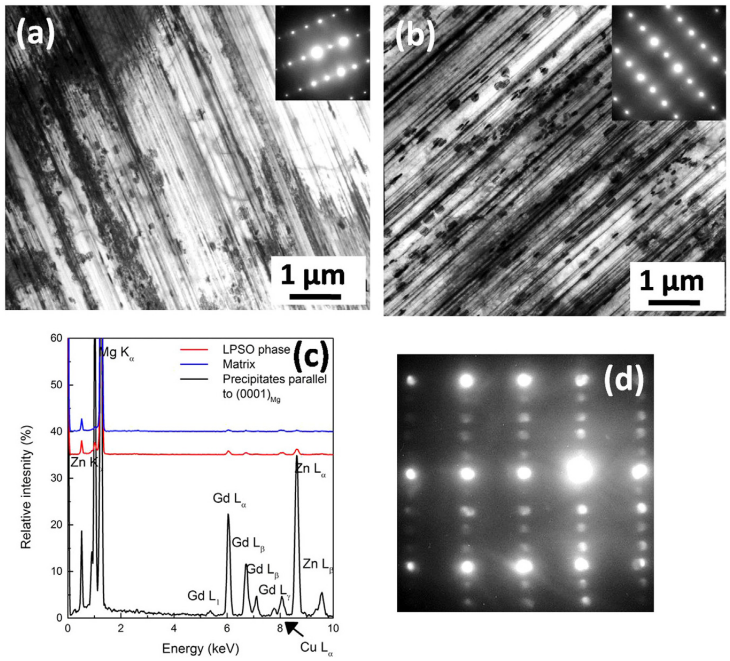

Figure 11: TEM micrographs of alloy 2: (a) subject to only temperature at 250 °C for 445 h (b) crept at 250 °C and 80 MPa (c) X-ray analysis of phases (d) SAD pattern of precipitates in crept alloy.

In contrast to the Mg_5Gd platelets found in alloy 1, the composition of these precipitates contained significant amount of Zn in addition to Gd, and are likely to be a ternary MgGdZn phase. The EDXS analysis and electron micro-diffraction patterns of the precipitates are shown in Fig. 11(c) and (d), respectively. However, a detailed analysis is required to confirm these precipitates.

4 Discussion

The intermetallic phase in Gd rich Mg–Gd–Zn alloys was termed as W–$Mg_3Zn_3Gd_2$ phase due to the compositional similarities to the W phase observed in Mg–Zn–Y systems [2,11,17–19]. Yamasaki et al. [8] identified with electron diffraction this phase as Mg_3Gd phase with the substitution of Zn atoms in the magnesium positions of the lattice. The results of the present study indicated a small difference in the lattice parameters of this phase in alloys 1 and alloy 2 (0.726 nm in alloy 1 and 0.732 nm in alloy 2) which may be due to the difference in the compositions of the phases: slightly higher Gd content was observed in alloy 1 whereas Zn/Gd ratio was 1.5 in alloy 2.

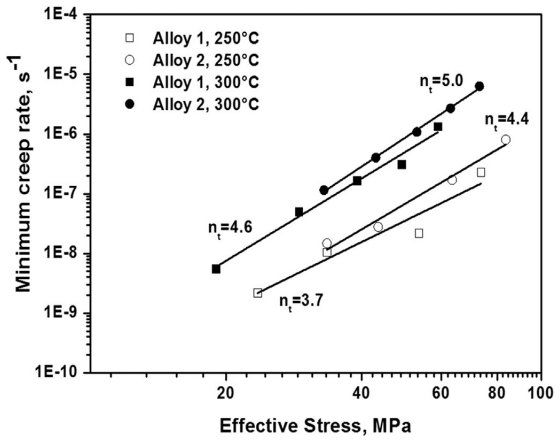

Figure 12: Minimum creep rates of the alloys plotted against effective stress $(\sigma - \sigma_{th})$.

The second phase, $(Mg,Zn)_3Gd$, forms in both alloys from the eutectic reaction. The microstructure investigation shows that the $(Mg,Zn)_3Gd$ solidified as a partially divorced eutectic. In addition to the grain boundary phase, LPSO phase was observed in both alloys. Mg–Zn–RE alloys are classified in to two groups according to the presence of LPSO phase in the literature: in type I alloys, the LPSO phase appears in the as cast structure as second phase (18 R type), and in type II alloys it forms during heat treatment (14 H type) [8].Mg–Zn–Y, Mg–Zn–Dy and Mg–Zn–Er are type I alloys whereas Mg–Zn–Gd and Mg–Zn–Tb are type II alloys.

However, recent studies reported the presence of LPSO phases in the as cast structure of Mg–Zn–Gd [10,11]. Zhang et al. [10] observed bulk LPSO phase at the boundaries along with the $(Mg,Zn)_3RE$ phase in a slow cooled permanent mould cast Mg–10Gd–3Y–1.8Zn alloy, and reported that the formation of such phase during solidification depends on the cooling rate. The solidification rates were not measured in the present study, but the coarse microstructure observed in the cast ingot indicates that the cooling rates were relatively slow and sufficient enough to form LPSO phase in Mg–10Gd–(2–6)Zn.

The post creep test microstructural analysis indicates the presence of coarse prismatic platelet precipitates, Mg_5Gd, in alloy 1 after creep tested at 250 °C as shown in Fig. 9(b). Even though the alloys were not solution treated but creep tested in the as cast condition, the dynamic precipitates observed in the present study after creep testing is related to the supersaturation of α-Mg during solidification under non equilibrium cooling conditions. Non equilibrium solidification resulted in solute segregation near the dendritic boundaries and up to 23 wt% Gd can soluble in Mg. The solute levels were thus higher than the solubility limit of

Gd and Zn at the creep deformation temperature near the interdendritic regions. Thus there was a driving force for the formation of precipitates from the supersaturated α-Mg. The applied creep stress enhanced the driving force and resulted in stress (or strain) assisted precipitation. It is likely that the dislocations generated during creep increased the heterogeneous sites for the nucleation of the precipitates. Since this additional driving force due to the creep deformation was absent in the heat treated sample, dynamic precipitation of Mg_5Gd did not take place (Fig. 9(a)).

In alloy 2, presence of ternary oval precipitates parallel to the LPSO phase was observed instead of Mg_5Gd. It is evident that the Zn content in Mg–Gd–Zn alloys influenced the type of precipitates that form during creep. Similar precipitates were reported earlier in Mg–RE– Zn based alloys [20,21]. Hnilica et al. [20] observed oval precipitates along the basal plane in the crept Mg–3Y–2Nd–1Zn–1Mn alloy. According to Smola et al. [21], even though such discs or spherical particles parallel to the basal planes are less effective in blocking the dislocation movement in the basal planes, they are strong obstacles that prevent cross slip of basal dislocations in non-basal planes. These results indicate that both alloys were strengthened by the dynamic precipitation during creep at 250 °C. The poor creep performance observed in the alloy 2 can be related to the dominant softening processes such as severe cracking at second phase as discussed later.

Creep of any metal is composed of two counteractive processes: strengthening and softening processes [22]. As long as the strengthening processes such as solid solution strengthening, precipitation hardening, strain hardening etc. dominate over the softening process such as coarsening of precipitates, cavitation, cross slip etc., the creep rate decreases. On the other hand, the creep rate increases when the softening process dominates. During steady state creep, both processes are opposing and balancing to each other [22]. In the present study, both alloys were solid solution strengthened initially by solute elements in the solid solution; alloy 1 had more solutes in the Mg matrix than that of alloy 2. As alloy 2 had higher Zn content, more Gd from the solid solution was removed and precipitated as second phase through eutectic reaction during solidification (Fig. 1(c)).

More solute in solid solution results in prolong primary region and lower minimum creep rate [23]: the longer primary region and one order lower minimum creep rate observed with alloy 1 creep deformed at 250 °C is attributed to the large solute supersaturation in the matrix. Due to the prolonged exposure at a temperature, the solute atoms precipitate and provide precipitation hardening. However, the large difference in creep behavior between two alloys was due to the volume fraction and type of precipitates. Similarly, the significant difference in creep behavior of the alloys with respect to the testing temperatures was due to the absence of the precipitates at higher testing temperature. The Gd solid solubility in magnesium increases with increase in temperature [24]. Additionally, the creep

exposure time might not be sufficient for the precipitation to take place as the alloy failed relatively earlier at 300 °C. Combined effects of these factors attributed to the absence of the dynamic precipitates during high temperature (300 °C) creep deformation, and hence showed poor creep performance.

Cracking along the LPSO phase at the bulk precipitates in the matrix was the likely softening process in both alloys. There was no appreciable difference in the volume fraction of precipitates between alloys. However, increase in stress or temperature increased the formation of the bulk ternary phase. Increasing the stress from 70 MPa to 80 MPa in alloy 1 resulted in higher density of crack along the bulk precipitates in the matrix (refer Fig. 6) which resulted in lower creep rupture life (Table 2). As seen in Fig. 6(f), the fracture region of alloy 1 contained more cracks in the matrix despite the higher volume fraction of finer precipitates suggesting that softening process dominated over the strengthening process due to the precipitate formation. In addition, cracking of grain boundary particles was also attributed to the failure. In case of alloy 2, the volume and morphology of grain boundary intermetallics played a major role to weaken the alloy.

The increase in the volume fraction and the continuous distribution of intermetallics resulted in easy crack initiation and propagation along the matrix-second phase interface (Fig. 7). Since the crystallographic lattices of Mg matrix (hcp) and the second phase (fcc) are different, it is difficult for the dislocations to pass through the intermetallic particles which results in dislocation pileup and eventually cracking [25,26]. Indirectly, these cracks facilitate easy removal of dislocations if otherwise, these dislocations pileups reduce the activity of dislocation sources [22].

High stress exponent values were observed in the present study (n = 6.8–8.8). Major creep mechanisms dominate in most of the magnesium alloys are dislocation creep and grain boundary diffusion with the n values around 5 and 1, respectively [4]. However, high n values (n value more than 5) are also reported for many magnesium alloys [27–31]. Mostly they are related to power law breakdown or a threshold stress is introduced as precipitates or reinforcements or dispersions present in the alloy interact with the moving dislocations and resist their movement (deformation) [27–30]. A stress exponent value of around 12 obtained for Mg-Y binary alloys was related to dislocation detachment from the solute atmosphere with the aid of applied stress [32]. Zhu et al. [33] attributed the stress exponent in the range of 6–9 obtained in Mg– RE alloys to dislocation creep. Dynamic precipitation was observed in their study, and claimed that they acted as effective dislocation barriers [33]. On the other hand, with particulate or fiber reinforced metal matrix composites or alloys in same studies, the high values of n are generally related to threshold stress arises from the reinforcements [34–37].

Recently, Garces et al. [37] related the high stress exponent value (n = 11) obtained for Mg97Y2Zn1 alloy to the composite nature of the alloy as hard LPSO

phase presented in the α-Mg matrix. These LPSO phase is expected to act as reinforcement fibers, and effectively carry the load during deformation which results in a threshold stress for the dislocations. In addition, presence of LPSO phase in the matrix decreases the stacking fault energy and hence increase creep resistance. Thus, the LPSO phases are effective obstacles for nonbasal slip [38].

To rationalize the high stress exponent obtained in the present study, a threshold stress analysis was performed. As suggested by Li and Langdon [39], the threshold stress, sth, could be obtained by extrapolation of double logarithmic plots of minimum creep rate over the applied stress to a value of 10^{10} s^{-1}. The values of sth for alloy 1 were 46.5 MPa at 250 °C and 31 MPa at 300 °C, whereas they were 36.5 MPa at 250 °C and 17 MPa at 300 °C for alloy 2. Fig. 12 shows the log–log plot of minimum creep rate vs. effective stress $\sigma_0 - \sigma_{th}$. The calculated 'n' values became 3.7–4.6 for alloy 1 and 4.4 to 5 for alloy 2 which are normally related to the dislocation creep. The prismatic platelets in alloy 1 and basal precipitates in alloy 2 formed during creep at 250 °C acted as effective barrier for the dislocation movement. Even though, dynamic precipitation was not observed during creep at 300 °C, similar 'n' values suggest that again dislocation creep was the rate controlling mechanism.

A high density of dislocations observed in between the LPSO phases (Fig. 9(d) and Fig. 10(b)) suggest that these LPSO phases in the basal plane also effectively restricted the dislocation movement in absence of precipitates. The activation energy for creep deformation, the Q value, provides more information about the exact creep mechanism. The calculated Q value for alloy 1 was $\approx$ 73.6–93.4 kJ/mol and the value was between 93 and 99 kJ/mol for the alloy 2. These values are lower than the activation energy for the diffusion of solutes atoms Zn and Mg atoms but close to that of Gd. The activation energy for the diffusion of Zn in magnesium and self-diffusion of magnesium are reported as 119 and 137 kJ/mol, respectively [40,41]. The activation energy for the diffusion of Gd in magnesium is 79–82 kJ/mol [42]. Also, these obtained Q values are close to the activation energy for the pipe diffusion of atoms, which involves diffusion of Mg atoms through dislocation core, 92 kJ/mol [43]. Hence for both alloys pipe diffusion and diffusion of Gd can be considered as the rate controlling creep mechanism at both 250 and 300 °C.

5 Conclusions

Among the two alloys studied, the as-cast microstructure of Mg–10Gd–6Zn alloy contained more volume of second phase ($(Mg,Zn)_3Gd$) at the interdendritic regions. The long LPSO phase was present in the matrixes of both alloys. Increase

in Zn content from 2% to 6% in Mg–10Gd–xZn alloy or test temperature from 250 to 300 °C significantly reduced the creep performance of the alloy.

Dynamic precipitation of prismatic platelets (Mg_5Gd) in Mg–10Gd–2Zn alloy and tiny oval precipitates (ternary precipitates) in basal planes in Mg–10Gd–6Zn alloy occurred respectively during creep at 250 °C. Increase in the test temperature (300 °C) deprived the strengthening from the dynamic precipitates in both alloys due to the higher solubility limit of Gd and Zn at high temperature.

Bulk shaped ternary precipitates formed along the LPSO phase on both the alloys and at all the testing conditions. These precipitates acted as a crack initiation sites during deformation. Additionally, higher volume fraction and continuous network morphology of second phase at the interdendritic regions facilitated easy crack initiation and propagation in Mg–10Gd–6Zn alloy resulted in poor creep performance.

Acknowledgments

The authors thank Mr. G. Meister for the preparation of alloys, Mrs. Petra Fischer and Mr. Gert Wiese for SEM investigations and Prof. Florian Pyczak and Mr. Uwe Lorenz for extending the TEM facilities. The Alexander von Humboldt (AvH) foundation is acknowledged by the first author for the post doctoral fellowship awarded to him. The first author also acknowledged CSIR-NIIST, India for deputing him to HZG, Germany.

References

1. B.L. Mordike, T. Ebert, Magnesium: Properties—applications—potential, Mater. Sci. Eng. A 302 (2001) 37–45.

2. J. Yang, L. Wang, L. Wang, H. Zhang, Microstructures and mechanical properties of Mg–4.5Zn–xGd (x = 0, 2, 3 and 5) alloys, J Alloy. Compd. 459 (2008)

3. A. Luo, M.O. Pekguleryuz, Cast magnesium alloys for elevated temperature applications, J. Mater. Sci. 29 (1994) 5259–5271.

4. M. Pekguleryuz, M. Celikin, Creep resistance in magnesium alloys, Int. Mater. Rev. 55 (2010) 197–217.

5. L. Yang, Y. Huang, F. Feyerabend, R. Willumeit, K.U. Kainer, N. Hort, Influence of ageing treatment on microstructure, mechanical and bio-corrosion

properties of Mg–Dy alloys, J. Mech. Behav. Biomed. Mater. 13 (2012) 36–44.

6. B.L. Mordike, Creep-resistant magnesium alloys, Mater. Sci. Eng. A 324 (2002) 103–112.

7. J.P. Li, Z. Yang, T. Liu, Y.C. Guo, F. Xia, J.M. Yang, M.X. Liang, Microstructures of extruded Mg–12Gd–1Zn–0.5Zr and Mg–12Gd–4Y–1Zn–0.5Zr alloys, Scr. Mater. 56 (2007) 137–140.

8. M. Yamasaki, M. Sasaki, M. Nishijima, K. Hiraga, Y. Kawamura, Formation of 14H long period stacking ordered structure and profuse stacking faults in Mg– Zn–Gd alloys during isothermal aging at high temperature, Acta Mater. 55 (2007) 6798–6805.

9. Y. Liu, G. Yuan, C. Lu, W. Ding, Stable icosahedral phase in Mg–Zn–Gd alloy, Scr. Mater. 55 (2006) 919–922.

10. S. Zhang, G.Y. Yuan, C. Lu, W.J. Ding, The relationship between $(Mg,Zn)_3RE$ phase and 14H LPSO phase in Mg–Gd–Y–Zn–Zr alloys solidified at different cooling rates, J. Alloy. Compd. 509 (2011) 3515–3521.

11. Y.J. Wu, X.Q. Zeng, D.L. Lin, L.M. Peng, W.J. Ding, The microstructure evolution with lamellar 14H-type LPSO structure in an Mg96.5Gd2.5Zn1 alloy during solid solution heat treatment at 773 K, J. Alloy. Compd. 477 (2009) 193–197.

12. G. Yuan, Y. Liu, C. Lu, W. Ding, Effect of quasicrystal and Laves phases on strength and ductility of as-extruded and heat treated Mg–Zn–Gd-based alloys, Mater. Sci. Eng. A 472 (2008) 75–82.

13. S. Zhang, G.Y. Yuan, C. Lu, W.J. Ding, Effect of Zn/Gd ratio on phase constitutions in Mg–Zn–Gd alloys, in: S.R.A. Wim H. Sillekens, Neale R. Neelameggham, Suveen N. Mathaudhu, (Eds.), Magnesium Technology 2011, Wiley Publications, California, USA, pp. 157–159.

14. J. Gröbner, A. Kozlov, X.-Y. Fang, S. Zhu, J.-F. Nie, M.A. Gibson, R. Schmid-Fetzer, Phase equilibria and transformations in ternary Mg–Gd–Zn alloys, Acta Mater. 90 (2015) 400–416.

15. A. Srinivasan, Y. Huang, C.L. Mendis, C. Blawert, K.U. Kainer, N. Hort, Investigations on microstructures, mechanical and corrosion properties of Mg– Gd–Zn alloys, Mater. Sci. Eng. A 595 (2014) 224–234.

16. A. Srinivasan, C. Blawert, Y. Huang, C.L. Mendis, K.U. Kainer, N. Hort, Corrosion behavior of Mg–Gd–Zn based alloys in aqueous NaCl solution, J. Magn. Alloy. 2 (2014) 245–256.

17. K. Liu, J. Zhang, L.L. Rokhlin, F.M. Elkin, D. Tang, J. Meng, Microstructures and mechanical properties of extruded Mg–8Gd–0.4Zr alloys containing Zn, Mater. Sci. Eng. A 505 (2009) 13–19.

18. K. Liu, J. Zhang, H. Lu, D. Tang, L.L. Rokhlin, F.M. Elkin, J. Meng, Effect of the long periodic stacking structure and W-phase on the microstructures and mechanical properties of the Mg–8Gd–xZn–0.4Zr alloys, Mater. Des. 31 (2010) 210–219.

19. J. Yang, W. Xiao, L. Wang, Y. Wu, L. Wang, H. Zhang, Influences of Gd on the microstructure and strength of Mg–4.5Zn alloy, Mater. Charact. 59 (2008) 1667–1674.

20. F. Hnilica, V. Janík, B. Smola, I. Stulikova, V. Ocenasek, Creep behaviour of the creep resistant MgY3Nd2Zn1Mn1 alloy, Mater. Sci. Eng. A 489 (2008) 93–98.

21. B. Smola, I. Stulikova, J. Pelcova, B.L. Mordike, Significance of stable and metastable phases in high temperature creep resistant magnesium – rare earth base alloys, J. Alloy. Compd. 378 (2004) 196–201.

22. M. Regev, A. Rosen, M. Bamberger, Qualitative model for creep of AZ91D magnesium alloy, Metall. Mater. Trans. A 32 (2001) 1335–1345.

23. S.M. Zhu, M.A. Gibson, J.F. Nie, M.A. Easton, G.L. Dunlop, Primary creep of diecast magnesium – rare earth based alloys, Metall. Mater. Trans. A 40 (2009) 2036–2041.

24. L.L. Rokhlin, Magnesium Alloys Containing Rare Earth Metals: Structure and Properties, Taylor & Francis, London, 2003.

25. D.K. Xu, L. Liu, Y.B. Xu, E.H. Han, Effect of microstructure and texture on the mechanical properties of the as-extruded Mg–Zn–Y–Zr alloys, Mater. Sci. Eng. A 443 (2007) 248–256.

26. D.K. Xu, W.N. Tang, L. Liu, Y.B. Xu, E.H. Han, Effect of W-phase on the mechanical properties of as-cast Mg–Zn–Y–Zr alloys, J. Alloy. Compd. 461 (2008) 248–252.

27. B. Jing, S. Yangshan, X. Shan, X. Feng, Z. Tianbai, Microstructure and tensile creep behavior of Mg–4Al based magnesium alloys with alkaline-earth elements Sr and Ca additions, Mater. Sci. Eng. A 419 (2006) 181–188.

28. I.P. Moreno, T.K. Nandy, J.W. Jones, J.E. Allison, T.M. Pollock, Microstructural stability and creep of rare-earth containing magnesium alloys, Scr. Mater. 48 (2003) 1029–1034.

29. S.M. Zhu, M.A. Easton, M.A. Gibson, M.S. Dargusch, J.F. Nie, Analysis of the creep behaviour of die-cast Mg–3Al–1Si alloy, Mater. Sci. Eng. A 578 (2013) 377–382.

30. S.M. Zhu, B.L. Mordike, J.F. Nie, Creep properties of a Mg–Al–Ca alloy produced by different casting technologies, Mater. Sci. Eng. A 483–484 (2008) 583–586.

31. N. Kashefi, R. Mahmudi, The microstructure and impression creep behavior of cast AZ80 magnesium alloy with yttrium additions, Mater. Des. 39 (2012) 200–210.

32. K. Maruyama, M. Suzuki, H. Sato, Creep strength of magnesium-based alloys, Metall. Mater. Trans. A 33 (2002) 875–882.

33. S.M. Zhu, M.A. Gibson, M.A. Easton, J.F. Nie, The relationship between microstructure and creep resistance in die-cast magnesium – rare earth alloys, Scr. Mater. 63 (2010) 698–703.

34. H. Dieringa, Y. Huang, P. Maier, N. Hort, K.U. Kainer, Tensile and compressive creep behaviour of Al_2O_3 (Saffil) short fiber reinforced magnesium alloy AE42, Mater. Sci. Eng. A 410–411 (2005) 85–88.

35. H. Dieringa, N. Hort, K.U. Kainer, Investigation of minimum creep rates and stress exponents calculated from tensile and compressive creep data of magnesium alloy AE42, Mater. Sci. Eng. A 510–511 (2009) 382–386.

36. H. Dieringa, Y. Huang, P. Wittke, M. Klein, F. Walther, M. Dikovits, C. Poletti, Compression-creep response of magnesium alloy DieMag422 containing barium compared with the commercial creep-resistant alloys AE42 and MRI230D, Mater. Sci. Eng. A 585 (2013) 430–438.

37. G. Garcés, E. Oñorbe, F. Dobes, P. Pérez, J.M. Antoranz, P. Adeva, Effect of microstructure on creep behaviour of cast Mg97Y2Zn1 (at%) alloy, Mater. Sci. Eng. A 539 (2012) 48–55.

38. D.D. Yin, Q.D. Wang, C.J. Boehlert, V. Janik, Y. Gao, W.J. Ding, Creep behavior of Mg–11Y–5Gd–2Zn–0.5Zr (wt%) at 573 K, Mater. Sci. Eng. A 546 (2012) 239–247.

39. Y. Li, T.G. Langdon, A simple procedure for estimating threshold stresses in the creep of metal matrix composites, Scr. Mater. 36 (1997) 1457–1460.

40. M. Suzuki, T. Kimura, J. Koike, K. Maruyama, Effects of zinc on creep strength and deformation substructures in Mg–Y alloy, Mater. Sci. Eng. A 387–389 (2004) 706–709.

41. H. Mehrer, Diffusion in Solid Metals and Alloys, Springer-Verlag Berlin Heidelberg, Berlin, 1990, Landolt-Börnstein-Group III Condensed Matter.

42. S.K. Das, Y.-B. Kang, T. Ha, I.-H. Jung, Thermodynamic modeling and diffusion kinetic experiments of binary Mg–Gd and Mg–Y systems, Acta Mater. 71 (2014) 164–175.

43. M. Celikin, M. Pekguleryuz, The role of α-Mn precipitation on the creep mechanisms of Mg–Sr–Mn, Mater. Sci. Eng. A 556 (2012) 911–920.